Cage-confinement of gas-phase ferrocene in zeolitic imidazolate frameworks to synthesize high-loading and atomically dispersed Fe–N codoped carbon for efficient oxygen reduction reaction†

Guanying Ye,[a] Qian He,[c] Suqin Liu,*[ab] Kuangmin Zhao,[a] Yuke Su,[a] Weiwei Zhu,[a] Rongjiao Huang[a] and Zhen He *[ab]

Fe–N codoped carbon (Fe–N/C) has emerged as one of the most promising non-precious electrocatalysts for the oxygen reduction reaction (ORR). However, the fabrication of Fe–N/C with high Fe and N loadings while maintaining atomic dispersion of the loaded Fe is still challenging. Herein, we present a cage-confinement synthesis strategy that utilizes zeolitic imidazolate framework-8 (ZIF-8) with an ordered microporous structure to uniformly adsorb gas-phase ferrocene (FeCp) molecules at mildly elevated temperatures followed by carbonization to fabricate Fe–N/C with a high content of atomically dispersed Fe and abundant N. The content of FeCp molecules adsorbed in the nanocavities of ZIF-8 could be precisely controlled by the adsorption temperature and time, and confining the adsorbed FeCp in the nanocavities of ZIF-8 could effectively prevent the Fe atoms from aggregating and/or forming Fe compounds during the carbonization process. The Fe–N/C fabricated under optimal conditions has a high iron loading of 5.86 wt% and abundant N content of 10.51 at%. The as-prepared Fe–N/C exhibits a remarkable ORR catalytic performance in 0.1 M KOH with a half-wave potential ($E_{1/2}$) of 0.85 V (vs. RHE) and excellent long-term durability (less than 10 mV change of $E_{1/2}$ after 10 000 cycles of the CV test and 11% current density decay after a 40 000 s long-term ORR test). This work provides a simple and controllable synthesis strategy for fabricating high-content atomically dispersed Fe and N codoped carbon catalysts, which might also shed light on the design and synthesis of other single-atom metal doped carbon materials for energy storage and conversion applications.

1. Introduction

The increasing energy and environmental crisis has urged the research on energy storage and conversion (e.g., batteries,[1–4] electroreduction/photoelectroreduction of CO_2 and N_2,[5–7] and photocatalytic degradation of pollutants[8]) to thrive. Among these, owing to its high energy density and eco-friendliness, the metal–air battery is considered an intriguing energy storage device toward sustainable development of human society.[9,10] However, the low coulombic efficiency of metal–air batteries caused by the sluggish kinetics of the oxygen reduction reaction (ORR) on the air cathodes needs to be improved urgently.[10] Although precious metal (PM) catalysts, especially Pt-group metal catalysts, exhibit high catalytic activities toward the ORR, the de ciencies of the PM catalysts, namely, high costs, resource scarcity, and inferior stability, have greatly limited their large-scale commercialization.[11,12] Therefore, it is critical to develop ORR catalysts with high efficiency and long term durability based on earth-abundant elements at low costs.

Recently, a wide variety of transition-metal-related materials (e.g., metal carbides,[13] oxides,[14–16] and sul des,[17] and composite materials) have been developed for oxygen electrocatalysis. Among these, metal–nitrogen codoped carbon (M–N/C, M refers to Fe, Co, Ni, etc.) materials have emerged as promising alter-natives to the PM catalysts as high-performance ORR electro-catalysts due to their unique electronic properties, low cost, and excellent catalytic performance.[18–22] In particular, extensive research has been devoted to fabricating nanostructured M–N/C catalysts with atomically dispersed metal sites, high speci c surface areas, and appropriate electronic properties to expose abundant active sites.[23] Although dispersion of metals at the atomic-scale in N doped carbon can be achieved by adopting

[a]College of Chemistry and Chemical Engineering, Central South University, Changsha, Hunan 410083, P. R. China. E-mail: zhenhe@csu.edu.cn; sqliu2003@126.com

[b]Hunan Provincial Key Laboratory of Chemical Power Sources, Central South University, Changsha, Hunan 410083, P. R. China

[c]Cardiff Catalysis Institute, School of Chemistry, Cardiff University, CF10 3AT Cardiff, UK

† Electronic supplementary information (ESI) available: Molecular modeling, HAADF-STEM and EDS mapping analysis, UV-vis characterization, particle size measurements, TEM characterization, XRD analysis, XPS analysis, electrochemical measurements, and ICP-OES data.

M–N/C catalysts with a high metal loading while maintaining atomic dispersion of the loaded metal. Although lowering the concentration of the metal sources during the synthesis could, to some extent, limit the aggregation of the doped metal atoms, it usually leads to a low content of M–N_x sites in the obtained M–N/C catalysts.[27] To the best of our knowledge, the metal loadings in most of the reported M–N/C catalysts with atomi-cally dispersed metal are below 4 wt%.[28] Iron–nitrogen codoped carbon (Fe–N/C) with Fe–N_x moieties has been regarded as a promising ORR catalyst among the M–N/C catalysts. Previous research has been devoted to improving the iron loading by adjusting the iron source and synthesis strategy; few studies could achieve a loading of atomically dispersed iron over 3 wt%.[25] In addition, the massive loss of nitrogen caused by the formation of inactive iron nitride and the decline of surface area resulting from the protonation effect of iron during the synthesis have led to a reduction in both the effective formation of the Fe–N_x sites and the amount of the exposed active sites.[26,29–34] Therefore, a facile and controllable strategy for the synthesis of high-performance Fe–N/C catalysts with, simulta-neously, a substantial loading of atomically dispersed Fe, abundant N doping, and a high speci c surface area is greatly desired.

Zeolitic imidazolate frameworks (ZIFs), a class of metal–organic frameworks (MOFs) with highly ordered porous struc-tures and abundant nitrogen,[35,36] have been widely used in gas storage/separation,[37–39] energy-related applications,[40–42] and catalysis. Metal sources introduced into the rigid skeletal structures of ZIFs could be trapped there, and thus migration and aggregation of the metal atoms are limited in further treatments.[26,43] Inspired by the gas adsorption features of ZIFs, metal sources with relatively low boiling or sublimation points could be turned into their gas phases at elevated temperatures and then adsorbed and stored in the porous structures of ZIFs.

Herein, we utilize ZIF-8 (i.e., a ZIF made of zinc ions coor-dinated with 2-methylimidazole rings) with abundant micro-pores as a cage to adsorb and con ne gas-phase ferrocene (FeCp) molecules to form a FeCp@ZIF-8 precursor, and further fabricate porous carbon enriched with N and atomically dispersed Fe by carbonization of the FeCp@ZIF-8 precursor. Our results demonstrate that this cage-con nement synthesis strategy could signi cantly increase the overall Fe loading in the nal carbon materials while effectively restricting the aggrega-tion of Fe and loss of N during the carbonization process. Besides, the amount of FeCp adsorbed into the ZIF-8 precursor could be facilely regulated by the partial pressure of the FeCp vapor via controlling the adsorption temperature and time. Owing to a high loading of the atomically dispersed Fe (5.86 wt%) and a high content of N (10.51 at%), the as-prepared Fe–N/C catalyst exhibits a competitive ORR catalytic perfor-mance with a half-wave potential of 0.85 V (vs. RHE) and limiting current density of 6.0 mA cm^{-2} in alkaline medium, which is superior to that of the commercial 20 wt% Pt/C catalyst.

2. Experimental

2.1 Materials

$Zn(NO_3)_2$\$6H_2O (>99.0%), 2-methylimidazole (>99.0%), and methanol (>99.5%) of AR grade were purchased from Sino-pharm Chemical Reagent Co., Ltd. $Fe(C_5H_5)_2$ (>98.0%) was purchased from Xiangzhong Chemical Reagent Research Institute. All the chemicals were used as received without further puri cation.

2.2 Synthesis

Synthesis of ZIF-8. 10 mmol of $Zn(NO_3)_2$\$6H_2O and 40 mmol of 2-methylimidazole were dissolved in 200 ml of methanol under vigorous stirring for 4 h and then the formed mixture was aged for 24 h at room temperature. A er ltration, the collected powdery product, i.e., ZIF-8, was washed with methanol three times and dried at 60 C in an oven overnight.

Synthesis of FeCp@ZIF-8. A 5 mL glass vial containing 40 mg of FeCp was placed in a 150 mL glass bottle containing 200 mg of the synthesized ZIF-8. The bottle was sealed tightly and placed at different temperatures (i.e., 80, 105, 130, and 155 C) for 9 h to obtain the FeCp loaded ZIF-8 samples. The FeCp loaded ZIF-8 samples were also prepared at 155 C with different adsorption times (from 1 to 9 h) to adjust the amount of Fe in the precursor.

Synthesis of N/C and Fe–N/C. The prepared ZIF-8 was carbonized in a tube furnace under an Ar/H_2 (90/10, v/v) ow. During the high-temperature pyrolysis process, the tempera-ture was rst raised from room temperature to 200 C at a rate of 5 C min^{-1} and then maintained at 200 C for 2 h. A er that, the temperature was further increased from 200 to 800 C at 5 C min^{-1} and maintained at 800 C for 2 h. Finally, the pyrolyzed product was treated in a 0.5 M H_2SO_4 solution for 12 h to remove the impurities (e.g., ZnO), and then collected by ltration, washed with deionized water, and dried overnight at 60 C in an oven to obtain the N/C sample. The Fe–N/C was obtained by carbonizing the pre-prepared FeCp loaded ZIF-8 in the same way. The Fe–N/C derived from different FeCp loaded ZIF-8 precursors that were prepared at different adsorption temperatures of 80, 105, 130, and 155 C are named as Fe–N/C-80, Fe–N/C-105, Fe–N/C-130, and Fe–N/C-155, respectively.

2.3 Characterization

Fourier transform infrared (FT-IR) spectroscopy was used to analyze the bonding states and compositions of the FeCp@ZIF-8 precursors in the range of 3200 to 400 cm^{-1} on a Nicolet-5700 spectrometer. Raman spectra were obtained from 200 to 3300 cm^{-1} on a Raman spectrometer (LabRAM HR, HORIBA). X-ray diffraction (XRD) patterns were obtained at the 2q angle of 5 to 80 at a scan rate of 5 min^{-1} by using Cu Ka radiation (l ¼ 0.15418 nm) on a Rigaku D/max 2500 X-ray diffractometer. The decomposition processes of the FeCp@ZIF-8 and ZIF-8 were characterized by thermogravimetric/differential thermal anal-ysis (TG/DTA) on a thermal analyzer (DTA-50) from room temperature to 900 C at a heating rate of 5 C min^{-1} in an Ar

atmosphere. The particle size distributions of N/C and Fe–N/C-155 were manually measured from SEM images based on at least 30 particles by using statistical so ware (nano measure-ment). Inductively coupled plasma optical emission spectrom-etry (ICP-OES, Optima 5300DV) was used to determine the Fe content in the samples. Low-pressure N_2 adsorption–desorption isotherms for the Brunauer–Emmett–Teller (BET) speci c surface area were recorded on an Autosorb-iQ (Quantachrome) analyzer at 77 K. The morphologies of the samples were inves-tigated by using a scanning electron microscope (SEM, FEI Nova™ NanoSEM230). The detailed structure and elemental analysis were investigated using a high-resolution transmission electron microscope (HRTEM, Bruker Nano GmbH Berlin Esprit, operated at 300.0 kV) equipped with an energy dispersive X-ray spectroscopy system (EDS, Bruker Nano GmbH Berlin Quantax). Aberration-corrected STEM characterization was carried out using a JEOL JEM-ARM200CF microscope operated at 200 kV. The UV-vis spectra of the samples were recorded to analyze the contents of FeCp and iron by using an UV-vis spectrometer (Shimadzu UV-1780) from 600 to 200 nm. An X-ray photoelectron spectroscopy (XPS) study was carried out on a ThermoFisher ESCALAB 250Xi spectrometer using an Al Ka source (1486.6 eV).

2.4 Electrochemical measurements

Rotating-disk electrode (RDE) measurements were carried out on an Autolab PGSTAT204 electrochemical workstation equip-ped with a RDE system to evaluate the catalytic performance of the as-prepared samples in a three-electrode con guration with a piece of Pt mesh (1 cm 2 cm) as the counter electrode and an Ag/AgCl (in 3.5 M KCl) electrode as the reference electrode in

a N_2- or O_2-saturated 0.1 M KOH aqueous solution. The working electrode, a glassy carbon (GC) RDE with a diameter of 5 mm loaded with the prepared catalysts, was prepared as follows. About 6 mg of the as-prepared catalyst was added into 0.95 ml of anhydrous ethanol, and then 50 ml of 5% Na on solution was added. The mixture was placed under ultrasonication for at least 30 min to form a homogeneous ink. Then, 8 ml of the ink was dropped on the surface of the GC disk of the RDE and dried at room temperature naturally. The loading of the catalyst was about 0.245 mg cm ^{2}. A linear sweep voltammetry (LSV) study
was performed by scanning the potential from 0.20 to 0.90 V (vs. Ag/AgCl) at a scan rate of 10 mV s ^{1} with diff erent rotating rates (i.e., 400, 625, 900, 1225, and 1600 rpm). A cyclic voltam-metry (CV) test was performed without electrode rotation in the same potential range but at a scan rate of 50 mV s ^{1} in a N_2- or O_2-saturated 0.1 M KOH aqueous solution. The commercial 20 wt% Pt/C (named as Pt/C for short) was tested under the same conditions for comparison.

The electron transfer number (n) per oxygen molecule for the oxygen reduction reaction was determined on the basis of the Koutecky–Levich (K–L) equations (eqn (1) and (2)),

$$1/j = 1/j_L + 1/j_K \quad (1)$$

$$j_L = Bu^{1/2} = 0.62nFC_0D_0^{2/3}n^{1/6}u^{1/2} \quad (2)$$

where j is the measured current density, B is the Levich constant determined from the slope of the K–L plot, j_L is the mass-transfer-limited current density, j_K is the kinetically limited current density, F is the Faraday constant (96 485 C mol ^{1}), C_0 is the initial O_2 concentration in the electrolyte (1.26 10 ^{6} mol cm ^{3}), D_0 is the diff usion coeffi cient of O_2 in 0.1 M KOH (1.93
10 ^{5} cm^2 s ^{1}), and u is the angular velocity of the electrode, rad s ^{1}. Besides, n is the kinematic viscosity of the electrolyte (0.01 cm^2 s ^{1}) and the constant 0.62 is adopted when the rotation rate is expressed in rad s ^{1}.

3. Results and discussion

In this work, ZIF-8 is used as a “cage” to adsorb and con ne the sublimated gas-phase FeCp molecules, forming the FeCp@ZIF-8 precursor. This cage-con nement synthesis strategy could realize controllable loading and atomic dispersion of iron in the nal product (i.e., Fe–N/C) of the subsequent high-temperature pyrolysis of the FeCp@ZIF-8 precursor (Scheme 1). In detail,
ZIF-8 possesses cage-like nanocavities (with an inscribed-sphere diameter of ca. 11 A and a diagonal distance of ca. 18 A) with relatively small apertures (ca. 6 A, see details in Fig. S1 in the ESI†), while FeCp has a low sublimation temperature (ca. 100 C) and a suitable molecular diameter (ca. 4.5 A). Thus, the solid-phase FeCp could be easily turned into its vapor phase at mildly elevated temperatures and then adsorbed into the nanocavities of ZIF-8. Besides, since the equilibrium partial pressure (or the concentration in the gas phase) of the FeCp vapor in the reactor is directly related to the temperature (i.e., a higher temperature corresponds to a higher equilibrium partial pressure), the FeCp@ZIF-8 precursors with diff erent FeCp loadings could be facilely synthesized by controlling the temperature during the FeCp-adsorption process. A er the pyrolysis of the FeCp@ZIF-8 precursor under an Ar/H_2 (v/v, 90/ 10) atmosphere at 800 C, porous Fe–N/C with a high loading of the atomically dispersed iron and rich nitrogen is obtained.

In order to demonstrate that FeCp has been successfully adsorbed into the microporous structure of ZIF-8, FT-IR spec-troscopy and TG/DTA characterization was carried out. The FT-IR spectrum (Fig. 1a) of FeCp@ZIF-8 (prepared at the adsorp-tion temperature of 155 C for 9 h) shows characteristic absor-bance peaks of not only ZIF-8 but also FeCp (e.g., at 2850 and 1640 cm ^{1}). The TG/DTA curves of the FeCp@ZIF-8 (Fig. 1b) show similar mass loss and endothermic characteristics as

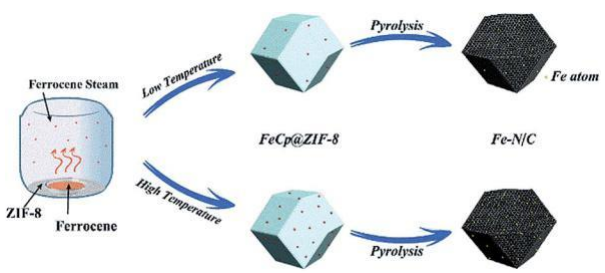

Scheme 1 Schematic illustration of the synthesis of Fe–N/C with diff erent Fe loadings by the cage-confinement synthesis strategy.

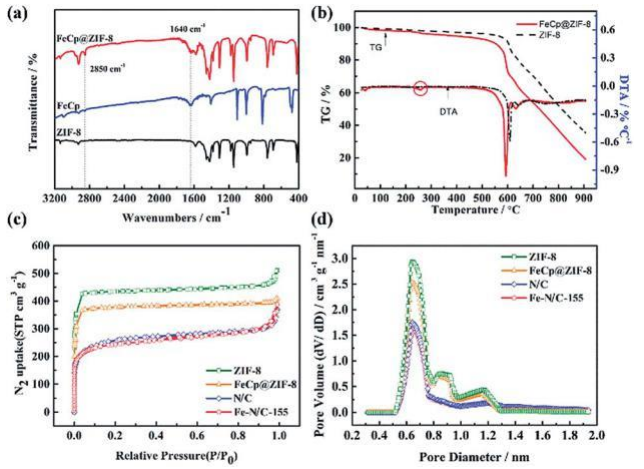

Fig. 1 (a) FT-IR spectra of ZIF-8, FeCp and FeCp@ZIF-8. (b) TG/DTA curves of ZIF-8 and FeCp@ZIF-8 heated under an Ar atmosphere from room temperature to 900 C at 5 C min ^{1}. (c) N_2 adsorption– desorption isotherms of ZIF-8, FeCp@ZIF-8, N/C, and Fe–N/C-155 and (d) their corresponding HK pore size distribution curves.

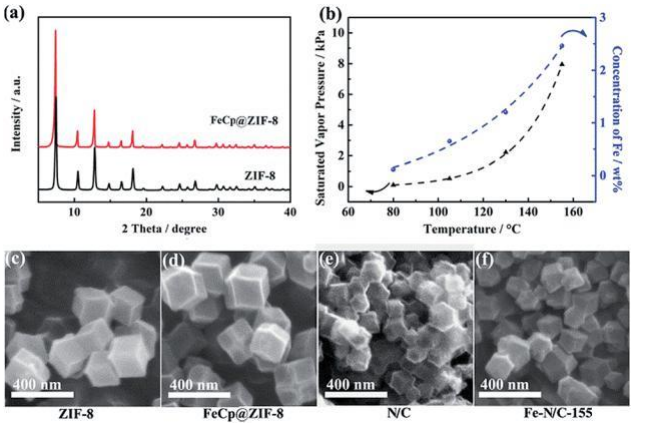

Fig. 2 (a) XRD patterns of ZIF-8 and FeCp@ZIF-8. (b) Saturated vapor pressure of FeCp (black triangles) and the content of Fe (measured by ICP-OES) (blue spheres) in FeCp@ZIF-8 as functions of the adsorption temperature. SEM images of (c) ZIF-8, (d) FeCp@ZIF-8, (e) N/C, and (f) Fe–N/C-155.

those of ZIF-8 except for an extra slight endothermic peak near 250 C, which is related to the boiling point of FeCp (i.e., 249 C). These results both suggest that FeCp has been adsorbed into ZIF-8.

To demonstrate that FeCp is adsorbed into the nanocavities of ZIF-8 rather than just on the outer surface, the speci c surface areas and pore structures of ZIF-8 and FeCp@ZIF-8 prepared at 155 C were measured by N_2 isothermal adsorption/desorption (Fig. 1c). The BET surface area of the FeCp@ZIF-8 (1486 m^2 g^{1}) is smaller than that of ZIF-8 (1676 m^2 g^{1}), and the volume of the pores between 0.6 and 1.2 nm in the FeCp@ZIF-8 analyzed by the Horvath–Kawazoe (HK) method is less than that in ZIF-8 (Fig. 1d), demonstrating that the FeCp is successfully encaged into the porous structure of ZIF-8. In addition, the EDS mapping images (Fig. S2†) of the FeCp@ZIF-8 show that Fe is uniformly distributed in the FeCp@ZIF-8 rather than around the periphery of the FeCp@ZIF-8 crystals, further demonstrating that the FeCp is con ned in the ZIF-8 cage instead of just being adsorbed on the outer surface. Moreover, the weight ratios of Fe in the FeCp@ZIF-8 before and a er being treated at 200 C for 2 h are similar, i.e., 2.46 and 2.49 wt%, respectively. This phenomenon suggests that the FeCp trapped in the ZIF-8 cage cannot escape easily.

XRD was used to characterize the crystal structure of the as-fabricated FeCp@ZIF-8 prepared at an adsorption temperature of 155 C for 9 h. The XRD pattern of the FeCp@ZIF-8 is almost identical to that of the pristine ZIF-8 (Fig. 2a), indicating that the adsorption of FeCp has no eff ect on the crystalline structure of ZIF-8. Since the saturated vapor pressure of a gas-phase component is directly related to the temperature, it is possible to control the amount of the adsorbed FeCp in the FeCp@ZIF-8 precursors at the adsorption equilibrium by adjusting the adsorption temperature. The Fe contents (measured by ICP-OES) in the FeCp@ZIF-8 precursors prepared at the adsorp-tion temperatures of 80, 105, 130, and 155 C are 0.12, 0.64, 1.20, and 2.46 wt%, respectively. Besides, the saturated vapor pressure of FeCp (calculated using the Clausius–Clapeyron equation) changes with the adsorption temperature in the same manner as the iron content in the FeCp@ZIF-8 precursors does, as shown in Fig. 2b. Based on the ICP-OES results, the average number of FeCp molecules that are accommodated in the ZIF-8 cage at diff erent adsorption temperatures could be calculated (as illustrated in Fig. S3†). These results all suggest that the iron content (i.e., the loading of FeCp) in the FeCp@ZIF-8 precursors could be precisely regulated by controlling the temperature of the FeCp adsorption process. Furthermore, at a certain adsorption temperature (e.g., at 155 C), the adsorption time could also be used to control the FeCp content in the FeCp@ZIF-8 precursor before the adsorption–desorption of FeCp reaches an equilibrium (Fig. S4†).

A SEM was used to study the eff ect of the adsorbed FeCp on the morphology of the ZIF-8 crystals. The FeCp@ZIF-8 precursor prepared at 155 C with the highest FeCp content in this work was used for comparison with the pristine ZIF-8. Unlike what has previously been reported in the literature regarding the introduction of iron sources leading to enlarged particle sizes and resulting in the decrease of the exposed speci c surface area of the obtained Fe-doped ZIF-8,[16,32,33] the SEM images of ZIF-8 and FeCp@ZIF-8 (Fig. 2c and d) show that both specimens display a similar dodecahedral morphology with a statistical average particle size of about 260 nm (Fig. S5a and b†), sug-gesting that the introduction of Fe into ZIF-8 through the adsorption of the vapor-phase FeCp into the nanocavities of ZIF-8 doesn't adversely aff ect the crystal growth of ZIF-8.

The as-synthesized ZIF-8 and FeCp@ZIF-8 prepared at 155 C were converted to N/C and Fe–N/C-155, respectively, via a high-temperature pyrolysis process. The obtained N/C and Fe–N/C-155 nanocrystals maintained the morphology of their corre-sponding precursor but with a smaller particle size (centered around 160 nm, Fig. 2e and f and S5c and d†). This phenom-enon might be caused by the decomposition of the MOF

skeleton and the escape of the gas-phase product,[31] leading to a shrunken particle size and porous structure for the carbonized products. Due to the similar particle sizes of N/C and Fe–N/C-155, the BET surface areas (i.e., 907 and 849 m^2 g^{-1}, respec-tively) and pore size distributions of N/C and Fe–N/C-155 are close (Fig. 1c and d). These results suggest that this cage-con nement synthesis could eff ectively prevent the surface area loss of the carbon catalyst while introducing metallic sites into it, providing an abundant accessible surface for catalysis.

HR-TEM and EDS mapping were carried out to characterize the distribution of elements in the carbonized products. The TEM studies demonstrate that the Fe–N/C-155 is amorphous and has a particle size similar to that of N/C (Fig. 3a and b). The TEM images of Fe–N/C-155 at diff erent magni cations show that there are no Fe particles observed (Fig. S6†). In addition, the HAADF-STEM image and the corresponding EDS mapping images of Fe–N/C-155 (Fig. 3c–f) show the uniform distribution of Fe and N. HAADF imaging with an AC STEM was used to visualize the dispersion of the Fe atoms in the Fe–N/C-155. As shown in Fig. 3g, the Fe atoms, identi ed by the bright dots marked with red cycles in the image, are atomically dispersed in this N-doped carbon material.

The crystalline structure of the Fe–N/C-155 was characterized by XRD. The XRD patterns of Fe–N/C-155 and N/C (Fig. 4a) both exhibit two broad diff raction peaks at about 25 and 44 , which are assigned to the (002) and (101) crystal planes of carbon, respectively.[44] No obvious characteristic diff raction peaks of Fe or Fe-based compounds (e.g., iron oxides, carbides, and nitrides) are detected by XRD. To explore whether Fe-based compounds, especially iron nitrides, were formed during

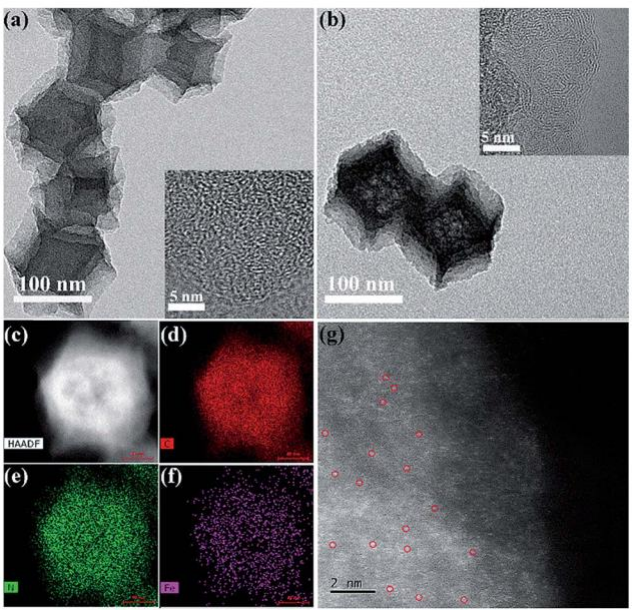

Fig. 3 TEM images of (a) N/C and (b) Fe–N/C-155 at various magni-fications (shown as the inset). (c) HAADF-STEM image of Fe–N/C-155 and its corresponding EDS elemental mapping analysis images of (d) carbon (red), (e) nitrogen (green), and (f) iron (purple). (g) HAADF image from an AC STEM image of Fe–N/C-155 (the Fe atoms are highlighted with red circles).

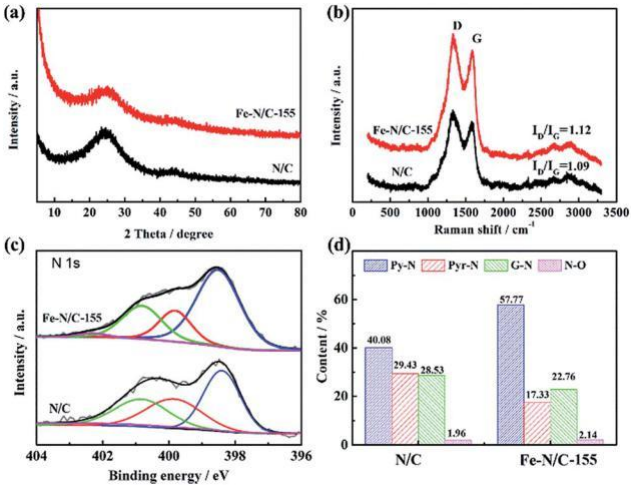

Fig. 4 (a) XRD patterns of N/C and Fe–N/C-155 before acid etching. (b) Raman spectra of N/C and Fe–N/C-155. (c) High-resolution N 1s XPS spectra of N/C and Fe–N/C-155. (d) The ratios of the four types of nitrogen in N/C and Fe–N/C-155.

calcination, the XRD patterns of the FeCp@ZIF-8 samples at diff erent pyrolysis stages (i.e., at diff erent temperatures) during the carbonization process were studied (Fig. S7†). Recent research has found that Fe species are usually formed above
500 C.[32] In this work, except for the diff raction peaks of ZnO, no characteristic diff raction peaks of iron or its compounds are observed in the samples pyrolyzed at 550, 600, and 700 C. This result shows that the iron-related compounds are probably not formed in the whole process of the material preparation, demonstrating that con ning Fe species in the “cage” of ZIF-8 can greatly prevent the agglomeration of Fe atoms and the formation of Fe-based compounds during the high-temperature carbonization. Moreover, this cage-con nement synthesis strategy could also increase the content of the atomically dispersed Fe in the Fe–N/C catalyst. The concentration of Fe in Fe–N/C-155 was tested by ICP-OES and the mass ratio of Fe was up to 5.86 wt%, which is higher than that of most reported isolated atomic Fe-doped carbon-based catalysts (Table S1†). This mass ratio of Fe is close to the theoretical content of iron that is calculated based on the adsorbed FeCp in the FeCp@ZIF-
8 precursor and the yield of the carbon product from the carbonization of ZIF-8 (see details in the ESI, Table S2†), sug-gesting that there is almost no loss of iron during the etching process. This result further veri es the superiority of this cage-con nement synthesis strategy to prevent the aggregation of the metal atoms and increase the metal loading in the nal carbon materials.

The eff ect of iron-doping on the porous carbon material was further analyzed by Raman spectroscopy and XPS. The Raman spectra of Fe–N/C-155 and N/C (Fig. 4b) both show two domi-nant peaks, i.e., the D band at 1330 cm^{-1} corresponding to the disordered carbon and the G band at 1585 cm^{-1} assigned to the sp^2-bonded graphitic carbon.[45] The intensity ratio of the D band to G band, I_D/I_G, of Fe–N/C-155 is slightly larger than that of N/ C, suggesting that Fe-doping might favor the formation of

disordered carbon during the pyrolysis.[46] The XPS studies were performed to clarify the surface chemistry including the contents and chemical states of C, N and Fe in Fe–N/C-155 (Fig. S8 and Table S3†). According to the literature,[30–32,47,48] the incorporation of Fe might cause a decrease of nitrogen (Table S4†). However, the atomic content of N in Fe–N/C-155 is 10.51%, nearly equivalent to that in N/C (10.24 at%). In most cases, the decline of N is due to the formation of Fe_3N,[24] whereas, in this work, by designing the cage-con nement synthesis strategy to precisely control the Fe content in the FeCp@ZIF-8 precursor, the nite iron atoms in each cavity are insufficient to form Fe_3N (supported by the XRD results). Moreover, the high resolution N 1s XPS spectra of Fe–N/C-155 and N/C (Fig. 4c) could be deconvoluted into four peaks, which are attributed to pyridinic-N (Py-N, 398.3 eV), pyrrolic-N (Pyr-N, 399.7 eV), graphitic-N (G-N, 400.8 eV) and oxidized-N (N-O, 402.5 eV).[49] The proportion of Py-
N in the total N of Fe–N/C-155 is signi cantly higher than that of N/C (Fig. 4d). As Py-N is recognized as an anchor point for Fe atoms, a higher content of Py-N could facilitate the formation of Fe–N_x active sites.[50,51] In addition, Py-N itself has also been demonstrated to be active toward the ORR.[52] This result further implies that our cage-con nement synthesis strategy can not only prevent the formation of iron-related agglomerates but also facilitate the retention of nitrogen in the produced carbon materials, which will be bene cial to the formation of the ORR active sites.

The ORR electrocatalytic performance of the as-prepared catalysts was rst evaluated by LSV in 0.1 M KOH on a RDE. As iron exerts a great in uence on the catalytic performance of the as-prepared Fe–N/C catalysts, the ORR catalytic perfor-mance of the Fe–N/C samples derived from the FeCp@ZIF-8 precursors with diff erent iron contents (adjusted by the adsorption temperature of FeCp) was tested (Fig. 5a and S9†). For a better comparison, the catalytic activities of the synthe-sized Fe–N/C catalysts are evaluated by measuring the half-wave
potential ($E_{1/2}$) and current density at 0.90 V vs. RHE ($j_{@0.9\ V}$). The relationship between their ORR catalytic performance (i.e., $E_{1/2}$ and $j_{@0.9\ V}$) and iron content is shown in Fig. 5b. The overall Fe contents based on the ICP-OES measurements are 0.18, 1.56, 3.20, and 5.86 wt% in the Fe–N/C samples derived from the FeCp@ZIF-8 precursors prepared at the adsorption tempera-tures of 80, 105, 130, and 155 C, respectively. Both $E_{1/2}$ and $j_{@0.9\ V}$ are increased as the iron content in the Fe–N/C increases. This result demonstrates the signi cance of developing a synthetic strategy to increase the iron loading at the atomic dispersion level in the Fe–N/C catalysts.

Among the Fe–N/C catalysts derived from the FeCp@ZIF-8 precursors prepared at diff erent adsorption temperatures, the Fe–N/C-155 shows the best catalytic performance for the ORR and therefore is selected for comparison with with the commercial 20 wt% Pt/C catalyst. The CV curves of the Pt/C, N/ C, and Fe–N/C-155 obtained in an O_2-saturated 0.1 M KOH solution all show prominent cathodic peaks at 0.80, 0.72 and 0.85 V, whereas the CV curves of these three samples obtained in a N_2-saturated electrolyte are featureless (Fig. 5c). In addi-tion, the $E_{1/2}$ on the LSV curve of Fe–N/C-155 is 0.85 V (Fig. 5d), which is more positive than that of both N/C (0.75 V) and Pt/C

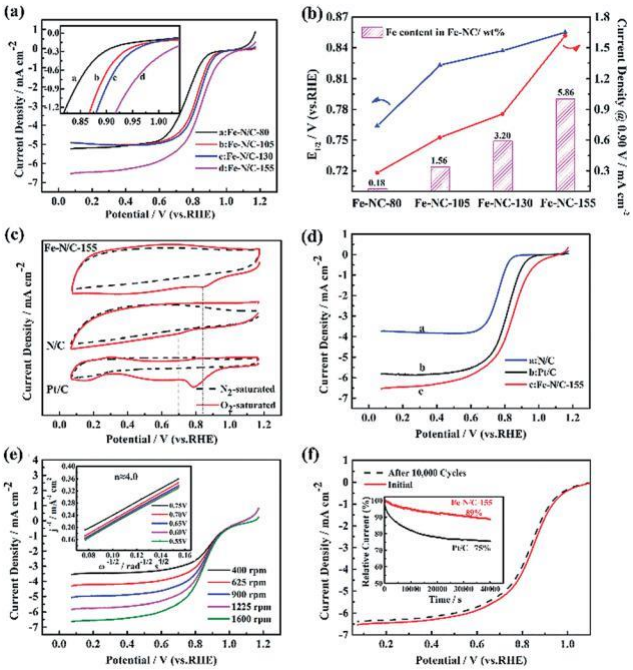

Fig. 5 (a) LSV curves of the Fe–N/C samples derived from the FeCp@ZIF-8 precursors prepared at diff erent adsorption temperatures at 1600 rpm. (b) Correlation between $E_{1/2}$, $j_{@0.9\ V}$, and the Fe content in the Fe–N/C samples. (c) CV curves of N/C, Fe–N/C-155, and Pt/C in a N_2- or O_2-saturated 0.1 M KOH solution. (d) LSV curves of N/C, Fe– N/C-155, and Pt/C in an O_2-saturated 0.1 M KOH solution at 1600 rpm.
(e) LSV curves of Fe–N/C at diff erent rotating rates and the K–L plots (shown in the inset) with the electron transfer number (n). (f) LSV curves of Fe–N/C-155 before and after 10 000 cycles obtained at 1600 rpm in an O_2-saturated 0.1 M KOH solution at room temperature. The inset shows the stability evaluation of Pt/C and Fe–N/C-155 tested at 0.60 V (vs. RHE) for 40 000 s.

(0.81 V). Meanwhile, the limiting current density (j_L) at 0.60 V on the LSV curve of Fe–N/C-155 is 6.0 mA cm^{-2}, which is higher than that of both N/C (3.8 mA cm^{-2}) and Pt/C (5.5 mA cm^{-2}). The as-prepared Fe–N/C-155 exhibited excellent ORR catalytic activity in alkaline medium and outperformed most of the re-ported iron-based ORR catalysts (Table S5†). The Kouteck´y– Levich (K–L) equation is used to calculate the electron transfer number (n) of the ORR on Fe–N/C-155 in the potential range from 0.75 to 0.55 V. The K–L plots exhibit excellent linearity and the estimated n is about 4.0, suggesting that the Fe–N/C-155 follows an apparent 4e reduction pathway for the ORR (Fig. 5e). The durability of the as-prepared Fe–N/C-155 under ORR conditions is evaluated by the long-term stability and accelerated durability test (ADT), as shown in Fig. 5f. The as-prepared Fe–N/C-155 shows only 11% current loss a er testing at 0.60 V for 40 000 s, whereas the commercial Pt/C suff ers a higher current loss of 25% under the same experi-mental conditions. The ADT was carried out by scanning the potential between 1.00 and 0.60 V for 10 000 cycles at a scan rate of 200 mV s^{-1} in O_2-saturated 0.1 M KOH. The Fe–N/C-155 exhibits an extremely subtle change (less than 10 mV) in $E_{1/2}$ compared to Pt/C (almost 40 mV, Fig. S10†). These results demonstrate that the Fe–N/C-155 catalyst with high contents of

atomically dispersed Fe and N is a promising non-precious metal electrocatalyst for the ORR in an alkaline electrolyte. In addition, compared to some classic synthetic methods (e.g., in situ co-precipitation and impregnation), our cage-con nement synthesis strategy not only provides a facile way to control the atomically dispersed iron-doping level but also realizes a higher iron loading in the MOF precursor with less consumption of the iron source, which is more economical (see details in the ESI, Fig. S11 and S12†). The above results strongly demonstrate that this rationally designed cage-con nement synthesis strategy could be effective for the fabrication of MOF-derived N-doped carbon materials with a high loading of atomically dispersed iron for highly efficient and stable ORR electrocatalysis.

4. Conclusions

In summary, a cage-con nement synthesis strategy for simultaneously achieving a high loading of atomically dispersed iron and a rich nitrogen content in MOF-derived carbon materials is developed. ZIF-8 with an ordered microporous structure is used as a cage host, and FeCp with a suitable molecular size and low sublimation temperature is used as the gas-phase adsorbate and Fe source. The FeCp@ZIF-8 precursors with a high content and uniform distribution of FeCp are obtained by adjusting the adsorption temperature and time, and are further converted to Fe–N/C with high Fe and N contents and large speci c surface areas. The nanocavities of ZIF-8 con ne the adsorbed FeCp molecules and effectively prevent the Fe atoms from aggre-gating during the carbonization process, which leads to a single-atom-like dispersion of Fe in the obtained Fe–N/C. The optimized Fe–N/C-155 catalyst exhibits a remarkable ORR catalytic performance in 0.1 M KOH with a more positive half-wave potential and superior durability compared to the commercial 20 wt% Pt/C. Considering the diversity of the cage hosts and guest adsorbates, the cage-con nement synthesis strategy developed in this work could be applicable for the design and fabrication of a series of MOF-derived M–N/C materials with highly dispersed metal sites for energy storage and conversion applications.

Conflicts of interest

There is no con ict of interest.

Acknowledgements

This work was supported by the National Natural Science Foundation of China (grant no. 51772332), the Hunan Provin-cial Science and Technology Plan Project (grant no. 2018RS3008 and 2017TP1001), the Natural Science Foundation of Hunan Province (grant no. 2018JJ2485), and the Innovation-Driven Project of Central South University (grant no. 2016CXS031). We thank the Diamond Light Source for access and support in the use of the electron Physical Science Imaging Centre (Instrument E01 with proposal number MG22766 and MG22776) that contributed to the results presented.

Notes and references

1 X. Feng, M. Ouyang, X. Liu, L. Lu, Y. Xia and X. He, Energy Storage Materials, 2018, 10, 246–267.
2 Q. Gan, H. He, K. Zhao, Z. He and S. Liu, J. Colloid Interface Sci., 2018, 530, 127–136.
3 Q. Gan, B. Liu, K. Zhao, Z. He and S. Liu, Electrochim. Acta, 2018, 279, 152–160.
4 N. Yabuuchi, K. Kubota, M. Dahbi and S. Komaba, Chem. Rev., 2014, 114, 11636–11682.
5 J. Ran, M. Jaroniec and S. Z. Qiao, Adv. Mater., 2018, 30, 1704649.
6 W. Zhu, K. Zhao, S. Liu, M. Liu, F. Peng, P. An, B. Qin, H. Zhou, H. Li and Z. He, J. Energy Chem., 2019, 37, 176–182.
7 Y.-C. Hao, Y. Guo, L.-W. Chen, M. Shu, X.-Y. Wang, T.-A. Bu, W.-Y. Gao, N. Zhang, X. Su and X. Feng, Nat. Catal., 2019, 2, 448–456.
8 L. Shi, Z. He and S. Liu, Appl. Surf. Sci., 2018, 457, 30–40.
9 Q. Yu, J. Xu, C. Wu, J. Zhang and L. Guan, ACS Appl. Mater. Interfaces, 2016, 8, 35264–35269.
10 Y.-P. Deng, Y. Jiang, D. Luo, J. Fu, R. Liang, S. Cheng, Z. Bai, Y. Liu, W. Lei, L. Yang, J. Zhu and Z. Chen, ACS Energy Lett., 2017, 2, 2706–2712.
11 S. Chen, J. Bi, Y. Zhao, L. Yang, C. Zhang, Y. Ma, Q. Wu, X. Wang and Z. Hu, Adv. Mater., 2012, 24, 5593–5597.
12 G. A. Ferrero, K. Preuss, A. Marinovic, A. B. Jorge, N. Mansor, D. J. L. Brett, A. B. Fuertes, M. Sevilla and M.-M. Titirici, ACS Nano, 2016, 10, 5922–5932.
13 Q. Wang, Y. Lei, Z. Chen, N. Wu, Y. Wang, B. Wang and Y. Wang, J. Mater. Chem. A, 2018, 6, 516–526.
14 J. Li, Z. Zhou, K. Liu, F. Li, Z. Peng, Y. Tang and H. Wang, J. Power Sources, 2017, 343, 30–38.
15 X. Zhang, R. Liu, Y. Zang, G. Liu, G. Wang, Y. Zhang, H. Zhang and H. Zhao, Chem. Commun., 2016, 52, 5946–5949.
16 Y. N. Wu, M. Zhou, S. Li, Z. Li, J. Li, B. Wu, G. Li, F. Li and X. Guan, Small, 2014, 10, 2927–2936.
17 B. Chen, R. Li, G. Ma, X. Gou, Y. Zhu and Y. Xia, Nanoscale, 2015, 7, 20674–20684.
18 U. I. Kramm, I. Herrmann-Geppert, J. Behrends, K. Lips, S. Fiechter and P. Bogdanoff, J. Am. Chem. Soc., 2016, 138, 635–640.
19 T. Liu, P. Zhao, X. Hua, W. Luo, S. Chen and G. Cheng, J. Mater. Chem. A, 2016, 4, 11357–11364.
20 Y.-J. Sa, D.-J. Seo, J. Woo, J.-T. Lim, J.-Y. Cheon, S.-Y. Yang, J.-M. Lee, D. Kang, T.-J. Shin, H.-S. Shin, H.-Y. Jeong, C.-S. Kim, M.-G. Kim, T.-Y. Kim and S.-H. Joo, J. Mater. Chem. A, 2016, 138, 15046–15056.
21 H. Yin, C. Zhang, F. Liu and Y. Hou, Adv. Funct. Mater., 2014, 24, 2930–2937.
22 D. Singh, K. Mamtani, C. R. Bruening, J. T. Miller and U. S. Ozkan, ACS Catal., 2014, 4, 3454–3462.
23 X. F. Yang, A. Wang, B. Qiao, J. Li, J. Liu and T. Zhang, Acc. Chem. Res., 2013, 46, 1740–1748.
24 Y. Chen, S. Ji, Y. Wang, J. Dong, W. Chen, Z. Li, R. Shen, L. Zheng, Z. Zhuang, D. Wang and Y. Li, Angew. Chem., Int. Ed., 2017, 56, 6937–6941.

25 Q. Liu, X. Liu, L. Zheng and J. Shui, Angew. Chem., Int. Ed., 2018, 57, 1204–1208.
26 L. Ma, S. Chen, Z. Pei, Y. Huang, G. Liang, F. Mo, Q. Yang, J. Su, Y. Gao, J. A. Zapien and C. Zhi, ACS Nano, 2018, 12, 1949–1958.
27 P. Yin, T. Yao, Y. Wu, L. Zheng, Y. Lin, W. Liu, H. Ju, J. Zhu, X. Hong and Z. Deng, Angew. Chem., Int. Ed., 2016, 55, 10800–10805.
28 Z. Li, D. Wang, Y. Wu and Y. Li, Natl. Sci. Rev., 2018, 5, 673–689.
29 Y. Deng, Y. Dong, G. Wang, K. Sun, X. Shi, L. Zheng, X. Li and S. Liao, ACS Appl. Mater. Interfaces, 2017, 9, 9699–9709.
30 Z.-Y. Wu, X.-X. Xu, B.-C. Hu, H.-W. Liang, Y. Lin, L.-F. Chen and S.-H. Yu, Angew. Chem., Int. Ed., 2015, 54, 8179–8183.
31 H. Zhang, S. Hwang, M. Wang, Z. Feng, S. Karakalos, L. Luo, Z. Qiao, X. Xie, C. Wang, D. Su, Y. Shao and G. Wu, J. Am. Chem. Soc., 2017, 139, 14143–14149.
32 Q. Lai, L. Zheng, Y. Liang, J. He, J. Zhao and J. Chen, ACS Catal., 2017, 7, 1655–1663.
33 J. Wang, G. Han, L. Wang, L. Du, G. Chen, Y. Gao, Y. Ma, C. Du, X. Cheng, P. Zuo and G. Yin, Small, 2018, 14, 1704282.
34 G. Ye, K. Zhao, Z. He, R. Huang, Y. Liu and S. Liu, ACS Sustainable Chem. Eng., 2018, 6, 15624–15633.
35 T. Palaniselvam, B. P. Biswal, R. Banerjee and S. Kurungot, Chem.–Eur. J., 2013, 19, 9335–9342.
36 Z. Liang, C. Qu, W. Guo, R. Zou and Q. Xu, Adv. Mater., 2017, 1702891.
37 L. Mu, B. Liu, H. Liu, Y. Yang, C. Sun and G. Chen, J. Mater. Chem., 2012, 22, 12246–12252.
38 S. Ma and H. C. Zhou, Chem. Commun., 2010, 46, 44–53.
39 D. Alezi, Y. Belmabkhout, M. Suyetin, P. M. Bhatt, Ł. J. Weselinski,´ V. Solovyeva, K. Adil, I. Spanopoulos, P. N. Trikalitis and A. H. Emwas, J. Am. Chem. Soc., 2015, 137, 13308–13318.
40 Q. Gan, K. Zhao, Z. He, S. Liu and A. Li, J. Power Sources, 2018, 384, 187–195.
41 Q. Gan, H. He, K. Zhao, Z. He and S. Liu, Electrochim. Acta, 2018, 266, 254–262.
42 K. Zhao, S. Liu, G. Ye, Q. Gan, Z. Zhou and Z. He, J. Mater. Chem. A, 2018, 6, 2166–2175.
43 J. Han, X. Meng, L. Lu, J. Bian, Z. Li and C. Sun, Adv. Funct. Mater., 2019, 1808872.
44 Q. Gan, J. Xie, Y. Zhu, F. Zhang, P. Zhang, Z. He and S. Liu, ACS Appl. Mater. Interfaces, 2018, 11, 930–939.
45 Y. Jiang, Z. He, Y. Li, J. Zhu, H. Zhou, W. Meng, L. Wang and L. Dai, Carbon, 2018, 127, 297–304.
46 P. Zhang, F. Sun, Z. Xiang, Z. Shen, J. Yun and D. Cao, Energy Environ. Sci., 2014, 7, 442–450.
47 Z. Huang, H. Pan, W. Yang, H. Zhou, N. Gao, C. Fu, S. Li, H. Li and Y. Kuang, ACS Nano, 2018, 12, 208–216.
48 Q. L. Zhu, W. Xia, L. R. Zheng, R. Zou, Z. Liu and Q. Xu, ACS Energy Lett., 2017, 2, 504–511.
49 R. Arrigo, M. H¨avecker, R. Schl¨ogl and D. S. Su, Chem. Commun., 2008, 40, 4891–4893.
50 A. Kong, X. Zhu, Z. Han, Y. Yu, Y. Zhang, B. Dong and Y. Shan, ACS Catal., 2014, 4, 1793–1800.
51 H. R. Byon, S. Jin and S. H. Yang, Chem. Mater., 2011, 23, 3421–3428.
52 D. Guo, R. Shibuya, C. Akiba, S. Saji, T. Kondo and J. Nakamura, Science, 2016, 351, 361–365.